Emergence of the nematic electronic state in FeSe

M. D. Watson,[1] T. K. Kim,[2] A. A. Haghighirad,[1] N. R. Davies,[1] A. McCollam,[3] A. Narayanan,[1] S. F. Blake,[1] Y. L. Chen,[1] S. Ghannadzadeh,[3] A. J. Schofield,[4] M. Hoesch,[2] C. Meingast,[5] T. Wolf,[5] and A. I. Coldea[1,*]

[1]*Clarendon Laboratory, Department of Physics, University of Oxford, Parks Road, Oxford OX1 3PU, United Kingdom*
[2]*Diamond Light Source, Harwell Campus, Didcot, OX11 0DE, United Kingdom*
[3]*High Field Magnet Laboratory, Institute for Molecules and Materials, Radboud University, 6525 ED Nijmegen, The Netherlands*
[4]*School of Physics and Astronomy, University of Birmingham, Edgbaston, Birmingham B15 2TT, United Kingdom*
[5]*Institute for Solid State Physics, Karlsruhe Institute of Technology, Germany*

We present a comprehensive study of the evolution of the nematic electronic structure of FeSe using high-resolution angle-resolved photoemission spectroscopy (ARPES), quantum oscillations in the normal state, and elastoresistance measurements. Our high-resolution ARPES allows us to track the Fermi surface deformation from fourfold to twofold symmetry across the structural transition at ~ 87 K, which is stabilized as a result of the dramatic splitting of bands associated with d_{xz} and d_{yz} character in the presence of strong electronic interactions. The low-temperature Fermi surface is that of a compensated metal consisting of one hole and two electron bands and is fully determined by combining the knowledge from ARPES and quantum oscillations. A manifestation of the nematic state is the significant increase in the nematic susceptibility approaching the structural transition that we detect from our elastoresistance measurements on FeSe. The dramatic changes in electronic structure cannot be explained by the small lattice distortion and, in the absence of magnetic fluctuations above the structural transition, point clearly towards an electronically driven transition in FeSe, stabilized by orbital-charge ordering.

I. INTRODUCTION

A nematic state is a form of electronic order that breaks the rotational symmetries without changing the translational symmetry of the lattice, and this state may play an important role in understanding high-temperature superconductivity. There has been great interest in determining such electron nematic states [1], most recently in iron-based superconductors [2]. Several scenarios have been proposed to explain the observed nematicity based on phonon-driven and electronically driven tetragonal symmetry breaking. As the lattice effects are very small and such a state is found in close proximity to a magnetic state, it has been suggested that the nematicity is generated by spin fluctuations and is a precursor of the incipient antiferromagnetic state [2]. Other models emphasize the tendency towards orbital order for the Fe d electrons in different local environments, resulting in the development of unequal occupancy of d_{xz} and d_{yz} orbitals, which drives the symmetry-breaking, and the magnetism is stabilized as a consequence [3]. Electronic nematic order can be revealed through strongly anisotropic resistivity and findings so far in iron-based superconductors have generally supported the spin-fluctuations scenario [4,5]. Understanding the dominant electronic interactions is of great importance, for they could determine the symmetry and properties of the superconducting state [2].

With a superconducting transition of $T_c \sim 9$ K, FeSe is a special case amongst Fe-based superconductors, since it undergoes a structural transition at $T_s \sim 87$ K but does not order magnetically at any temperature. It has also attracted a lot of interest due to the strong increase in T_c to 37 K under pressure [6], the existence of high-T_c intercalates of FeSe [7], and the fact that a monolayer of FeSe grown on $SrTiO_3$ could have its superconducting transition temperature in excess of 100 K [8]. The availability of high-quality bulk crystals, grown using chemical vapor transport [9], have recently reopened investigations into the electronic properties of FeSe. ARPES has found evidence of a large band splitting caused by orbital ordering below the structural transition [10,11] but the resolution of the available data cannot clarify the changes that occur at the Fermi level. Moreover, quantum oscillation experiments at low temperatures have detected an unusually small Fermi surface [12,13]. As magnetic fluctuations are detected only below the structural transition in FeSe, it is expected that they are not the driving force for this transition [14,15]. Thus the nature of the structural transition in FeSe is rather unusual and how the electronic structure is stabilized by breaking of the rotational symmetry could be the key to understanding its superconductivity and how it can be further enhanced.

In this paper, we explore the electronic structure of FeSe by using high-resolution ARPES, quantum oscillations and elastoresistivity measurements on the same batch of high-quality FeSe single crystals. These techniques provide a comprehensive picture of the evolution of the electronic structure of FeSe from the high-temperature tetragonal phase through the fourfold-symmetry-breaking structural transition at T_s and into the electronic nematic phase. We observe a strong in-plane d-wave-like deformation of the Fermi surface from fourfold to twofold symmetry as a result of the splitting of bands with d_{xz} and d_{yz} character. A direct manifestation of a nematic

*Corresponding author: amalia.coldea@physics.ox.ac.uk

Fermi surface of FeSe is the significant increase in the nematic susceptibility measured by elastoresistance measurements when approaching T_s, not emerging due to anisotropic magnetic fluctuations but being driven by the orbital/charge degrees of freedom. The low-temperature Fermi surface, based on our high-resolution data from ARPES and quantum oscillations, consists of an in-plane distorted quasi-two-dimensional hole band and two electron bands; the inner electron pocket is extremely elongated and quasi-two-dimensional, whereas the outer electron band, with predominantly d_{xy} character, is not detected by ARPES but is present in quantum oscillations. The high-temperature bands have orbital-dependent band renormalisations, with respect to band structure calculations due to many-body interactions, which are particularly significant for the d_{xy} band; this leads to a significant shrinkage of the Fermi surfaces (a factor of $\sim$5, compared with calculations). Our measurements also detect the band splitting induced by spin-orbit coupling ($\sim$20 meV at the Γ point).

II. EXPERIMENTAL DETAILS

Samples were grown by the $KCl/AlCl_3$ chemical vapor transport method. Magnetotransport measurements were performed as function of in-situ rotation in high magnetic fields up to 33 T at HFML in Nijmegen, using an excitation current of 0.8 mA. Good electrical contacts were achieved by using In solder. Quantum oscillations were observed in more than three samples with good agreement. ARPES measurements were performed at the I05 beamline of Diamond Light Source, UK. Single-crystal samples were cleaved *in situ* in a vacuum lower than 2×10^{-10} mbar and measured at temperatures ranging from 6–120 K. Measurements were performed using linearly polarized synchrotron light from 20–120 eV and employing Scienta R4000 hemispherical electron energy analyser with an angular resolution of 0.2–0.5 deg and an energy resolution of 3 meV. Elastoresistance measurements were performed by measuring the in-plane anisotropic transport properties while straining the crystals along the [110] direction in the tetragonal phase, by applying a voltage to a piezoelectric stack, similar to those discussed in Ref. [5] and detailed in Fig. 9 in the Appendix. Band-structure calculations were performed in WIEN2K using the GGA approximation with spin-orbit coupling included. Since FeSe does not show magnetic order, ARPES spectra are compared to non-spin-polarized band structure, with the relaxed lattice parameters $a = 3.7651$ Å, $c = 5.5178$ Å, and $z_{Se} = 0.241\,28$ [16] (see also Fig. 7 in the Appendix).

III. TEMPERATURE DEPENDENCE OF THE HOLE BANDS

Figure 1(a) shows the calculated Fermi surface of FeSe in the tetragonal paramagnetic phase, which consists of three hole pockets (α, β, and γ) around the Brillouin zone center (Γ) and two electronlike pockets (δ and ϵ), similar to other reports [17]. The bands, which cross the Fermi level, have mainly d_{xz}, d_{yz}, and d_{xy} character [Figs. 1(a) and 1(b)]. Due
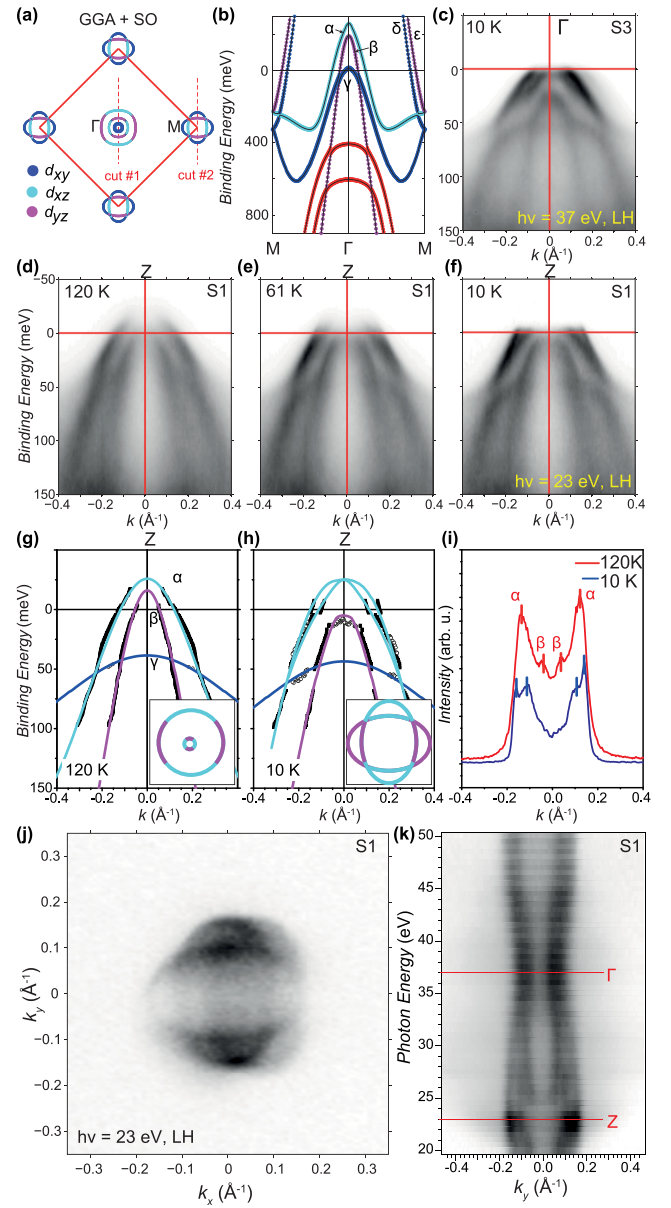

FIG. 1. (Color online) Temperature dependence of the hole bands in FeSe. (a) and (b) Band-structure calculation of the Fermi surface of FeSe in the tetragonal phase, projected into the $k_z = 0$ plane and colored by the dominant orbital character; the high-symmetry cuts are indicated. Calculations predict three hole pockets around the Γ point and two electron pockets around the M point. (c) The high-symmetry M-Γ-M cut (cut 1) at low temperature (10 K). (d)–(f) The temperature dependence of the A-Z-A cut at the Z point ($k_z = \pi/c$ plane). (g) and (h) Extracted band dispersion from constrained multiple Lorentzian fits to momentum-distribution curves (MDC, solid symbols) or peaks in the energy dispersive cut (EDC, open symbols) from the data in (d) and (f). The solid lines in (g) are the renormalized band structure from (a). The insets show a schematic Fermi surface. (i) MDC for the hole bands (α and β) at high and low temperatures. At 10 K, the α splits near the Fermi level, resulting in two crossings due to formation of twin domains. (j) Fermi surface map at 10 K indicating the elongation of the hole pocket combined with a duplicate rotated by $90°$ caused by twin domains. (k) Photon-energy dependence of the MDC at E_F (equivalent to scanning k_z in the Γ-Z direction) that shows a quasi-two-dimensional hole band at 10 K.

to the matrix elements effects in ARPES experiments the light polarization and the scattering geometry allows us to select mainly either d_{xz} or d_{yz} bands using LH (p) or LV (s) polarization, respectively, and to identify the orbital character of the measured bands, as shown in Fig. 5 and detailed in Ref. [18].

Figures 1(d)–1(f) show the evolution of the hole bands by performing high-symmetry cuts, either through M-Γ-M ($k_z = 0$) or A-Z-A ($k_z = \pi/c$), as shown in Figs. 1(c)–1(f) as a function of temperature. In the high-temperature tetragonal phase with preserved C_4 rotational symmetry, both α and β bands cross the Fermi level at the Z point, as shown by the Fermi-level momentum distribution curves (MDCs) at 120 K in Fig. 1(i). The degeneracy between the α and β bands is lifted by the spin-orbit coupling [19], which we can directly estimate from our data as being $\Delta_{SO} \sim 20$ meV, similar to results reported for LiFeAs [20]. On lowering the temperature below the structural transition at $T_s \sim 87$ K [Fig. 1(f)], the β band at Z is pushed below the Fermi level, as shown in Fig. 1. About 50 meV below the Fermi level, we also detect the presence of a broad band that is the d_{xy} band, γ, in Fig. 1(g), having weaker intensity due to matrix elements and being shifted significantly in relation to the band structure calculations for the tetragonal structure in Fig. 1(b). The effect of the loss of C_4 rotational symmetry through the structural transition from tetragonal to orthorhombic symmetry at T_s is clearly observed in the detailed Fermi surface map at the Z point, showing that the α pocket elongates to become elliptical, shown in Figs. 1(h) and 1(j). Due to the natural twinning of the samples, however, we observe two ellipses [in Fig. 1(h)] rotated 90° with respect to each other. The k_z dependence can be determined by measuring the Fermi-level MDC as a function of incident photon energy, shown in Fig. 1(k); we detect a quasi-two-dimensional shape for the α hole pocket, the only hole band that crosses the Fermi level at low temperature. The experimental area for the hole bands, A_k at 120 K is strongly reduced by a factor 5, as compared with band-structure calculations in the tetragonal phase (see Fig. 7) and we will later discuss the consistency with our quantum oscillations results at low temperatures (see Table I).

The effect of electronic correlations can be estimated by comparing band structure calculations with the band dispersion in the tetragonal phase at 120 K, as shown in Fig. 1(g). The obtained band renormalization factors for FeSe are ∼3.2, 2.1, and 8 for the α, β, and γ pockets, respectively, suggesting particularly strong orbital-dependent electronic correlations on the γ band with d_{xy} orbital character. These values are close to those reported for FeSe in Ref. [17], whereas in the case of FeSe$_x$Te$_{1-x}$, the band-selective renormalization varies strongly with values between 1 and 17 [21], the significantly higher value being assigned to the d_{xy} band. Band structure calculations including correlations (DMFT) on FeSe [22] give band renormalizations of ∼2.8 for the $d_{xz/yz}$ orbitals, comparable to the measured values, whereas the predicted value of ∼3.5 for the d_{xy} band is smaller than in experiments.

IV. TEMPERATURE DEPENDENCE OF THE ELECTRON BANDS

We now focus on the temperature dependence of the electron bands in FeSe shown in Fig. 2(a), visualizing the dramatic changes occurring through the structural transition. In the high-temperature tetragonal phase of FeSe, band-structure calculations predict two cylindrical electron pockets, as shown in Figs. 1(a) and 2(b). The outer electron band (labelled δ) has a dominant d_{xy} character whereas the inner electron band (labelled ϵ) has $d_{xz/yz}$ orbital character. At high temperatures (120 K), the inner $d_{xz/yz}$ band has a strong intensity at the M point, where bands disperse both along and perpendicular to the cut direction and are fourfold degenerate, as shown in Fig. 2(a). However, a combination of low intensity caused by matrix element effects for the d_{xy} orbital [18], as well as broadening due to either impurity scattering [23] or strong correlations may cause band incoherence [22,24] and difficulty to observe the d_{xy} band in ARPES at the M point [11,25,26].

Following the temperature dependence of the inner electron bands with $d_{xz/yz}$ orbital character, in the experimental Γ-M-Γ cut [cut 2 in Fig. 1(a)], the band crossing the Fermi level would have d_{yz} character, whereas the downwards dispersing band from the M point would have d_{xz} character [see Fig. 2(c)]. Below the structural transition that breaks the C_4 rotational symmetry, we observe a large band splitting, which can only occur if the $d_{xz/yz}$ degeneracy is broken and the d_{xz} and d_{yz} orbitals develop an unequal occupation.

As a result, the d_{yz} band moves up [ϵ_1 in Fig. 2(d)], and the d_{xz} band moves down (solid lines), but for the other structural domain the opposite occurs, the d_{xz} band moves up and the d_{yz} (ϵ_2) moves down indicated by the dashed lines in Fig. 2(d) and further detailed in Fig. 6 in the Appendix (x and y are defined in the *experimental* coordinate frame). This picture is consistent with that suggested from ARPES studies on detwinned crystals of FeSe [11], but the high resolution of our data allows us to detect the precise changes in the Fermi surface across the transition. The large band splitting of ∼50 meV at the M point at 10 K [Fig. 2(e)] indicates the lifting of of d_{xz} and d_{yz} degeneracy in FeSe. This was also observed in NaFeAs and BaFe$_2$As$_2$ over a very limited temperature range between the structural transition and magnetic transition [18,27–29]. In FeSe, this dramatic energetic shift observed below T_s is much larger than that expected from a simple structural orthorhombic distortion of 2×10^{-3} [$(a - b)/(a + b)$], which would cause a 17 meV shift in the absence of the renormalization effects (see Fig. 7). At the Fermi level, the resulting electron pocket is strongly elongated, with a $k_F(y) \approx 0.02$ Å^{-1} and $k_F(x) \approx 0.14$ Å^{-1}. However, due to twinning, the Fermi surface consists of two ellipses at 90° to each other, resulting in a cross-shaped Fermi surface [Fig. 2(f)], similar to the hole pocket. The degree of Fermi surface distortion is measured by the temperature dependence of k_F, and the ellipticity $k_F(y)(\varepsilon_1)$, shown in Fig. 4(l), is suggestive of an order parameter of a second-order phase transition at T_s. Thus the observed experimental elongation of both the electron and hole pockets at low temperatures in FeSe can be thought of as a consequence of the electronic anisotropy
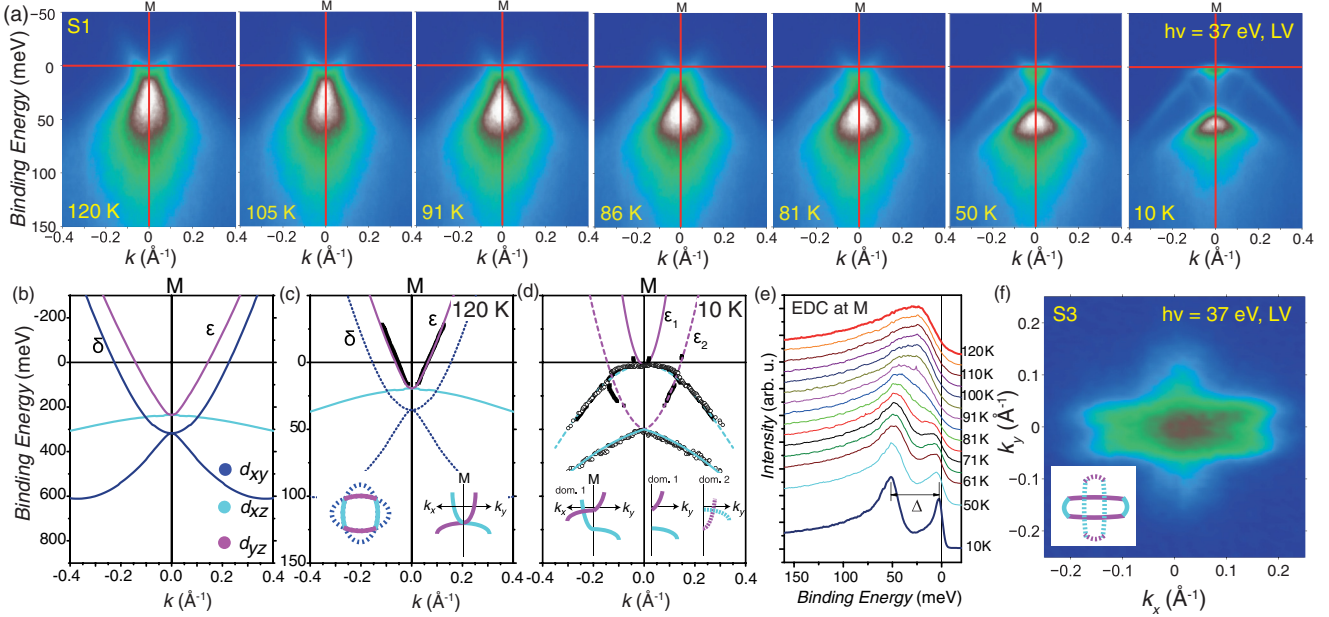
FIG. 2. (Color online) Development of a strongly elongated electron Fermi surface through the structural transition. (a) Temperature dependence of high-symmetry cut through M, showing the development of a splitting of intensity, which results from strong orbital-dependent shifts of the band structure with onset at $T_s = 87$ K. (b) The calculated band dispersions in the tetragonal structure. (c) The experimental band structure at 120 K (solid dots) renormalized to the high-temperature data (solid lines); the outer d_{xy} electron band (δ) is not observed at all at the M point. (d) The lifting of $d_{xz/yz}$ degeneracy at 10 K and the consequent band shifting for two different domains, ϵ_1 and ϵ_2, indicated by the solid and dashed lines, respectively. The insets show the schematic band dispersion for different domains and directions, as detailed in Fig. 6. (e) Temperature dependence of the EDC at the M point, showing the development of the splitting of bands with d_{xz} and d_{yz} character; the splitting Δ is plotted in Fig. 4(m). (f) Fermi surface map (integrated within 2 meV of the Fermi level) showing the cross-shape arising from strongly elongated Fermi surfaces at M in the two domains, shown schematically in the inset.

induced by orbital ordering in the presence of interactions. Another possible scenario for this behavior can be thought as a Pomeranchuk instability [30] that results in the spontaneous deformation of the Fermi surface from a fourfold symmetric almost circular shape at high temperature to an elliptical shape at low temperatures. In either case, this electronically induced Fermi surface deformation is also supported by the small specific heat jump at T_s compatible with an electronic contribution [9].

V. COMPARISON WITH QUANTUM OSCILLATIONS

In order to provide a complete and consistent picture of the Fermi surface of FeSe, we have also measured quantum oscillations in samples from the same batch used in the ARPES experiments. Quantum oscillations are a powerful technique that allows precise determination of cross-sectional areas of the Fermi surface and the corresponding orbitally averaged quasiparticle masses but it usually needs to rely on band structure or ARPES to provide the exact k-space location of these orbits. Magnetotransport measurements are performed in the normal state of FeSe at very low temperatures and high magnetic fields, as shown in Fig. 3(a). The oscillatory signal, periodic in $1/B$, is made clear by subtracting a high-order polynomial from the raw data in Fig. 3(b). The fast Fourier transform of ρ_{osc} shown in Fig. 3(c), identifies four different quantum oscillation frequencies, labelled F_{1-4} in ascending

order, that are directly linked to the extremal areas on the Fermi surface by the Onsager relation, $F_i = A_{ki}\hbar/(2\pi e)$, for a particular field orientation. All frequencies are lower than 1 kT in agreement with previous reports [12,13]. This is smaller than the frequencies of other iron-based superconductors that do not show any Fermi surface reconstruction, such as LaFePO [31] or LiFeAs [32]. Band-structure calculations predict the existence of five different quasi-two-dimensional cylinders with sizes (1–2.6 kT), much larger than those found in experiments (below 1 kT) (see Fig. 8 in the Appendix). The angular dependence of these frequencies also suggest a quasi-two-dimensional nature of these bands [see that the angular dependence of frequencies varies almost like $1/\cos\theta$ in Fig. 3(f)], and previous studies have suggested that at low temperatures FeSe has either only quasi-two-dimensional electron bands or electron and hole bands [12].

The cyclotron-averaged effective masses of the quasiparticles, extracted from the temperature dependence of the quantum oscillations amplitudes [Fig. 3(d)] for each orbit, are listed in Table I. We find a reasonably good agreement between the values of the effective masses for our different samples with those reported previously in Refs. [12,13]. The F_2 and F_4 orbits have similar effective masses of around 4 m_e, which may indicate that they originate from the same band, but with different k_z values, as in the case of a corrugated quasi-two-dimensional band, whereas the F_3 orbit has a particularly heavy effective mass of $\sim7(1)$ m_e, in agreement with other
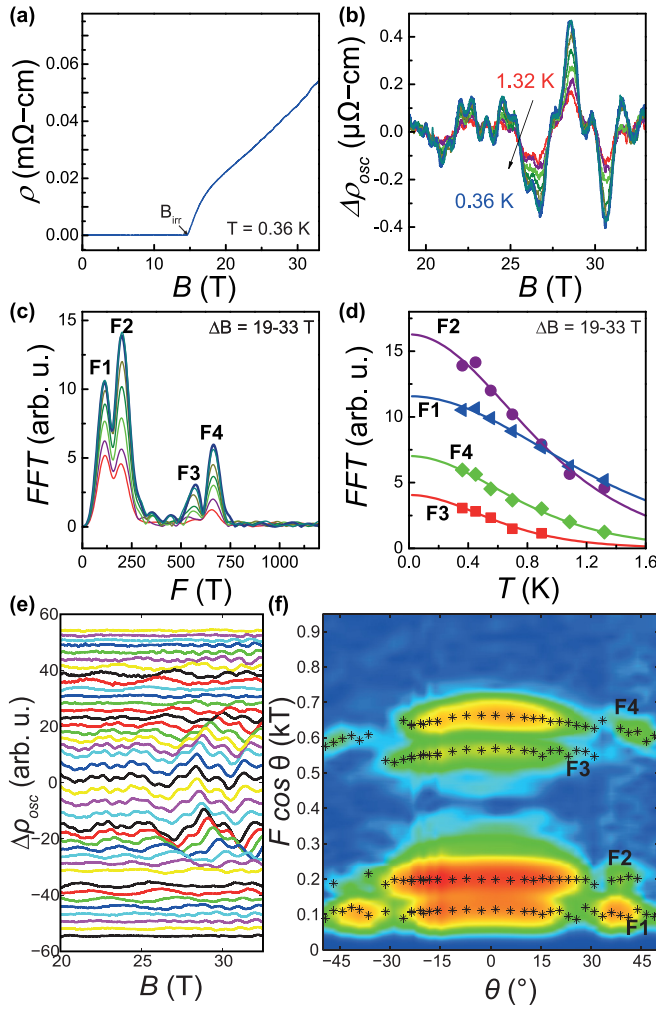
FIG. 3. (Color online) Quantum oscillations in FeSe. (a) Magnetoresistance of FeSe for a field applied along the c axis ($\theta = 0$) with the irreversibility field, B_{irr} around 14 T at 0.36 K. (b) The oscillatory part of the resistivity $\Delta\rho_{\mathrm{osc}}$, obtained by subtracting a polynomial background from the raw data. (c) Fourier transform (FFT) of the data in (b) identifying four different frequencies F_{1-4}, corresponding to k-dependent extremal areas on the Fermi surface. (d) Temperature dependence of the amplitude of oscillation, from which the effective masses may be extracted. (e) Quantum oscillations and (f) the corresponding Fourier transforms as a function of angle θ of applied magnetic field with respect to the c axis at 0.36 K. By plotting $F\cos\theta$ against θ one can identify if orbits correspond to a maximum or minimum of a quasi-two-dimensional Fermi surface. Color bar corresponds to the Fourier transform amplitude.

reports [12]. However, in the case of the F_1 pocket there is a variation of the quasiparticle masses between 0.7(2) [13] to 3(1) m_e. The strong disparity between the lighter masses F_1 and the heavier masses of F_4 points towards different band origin for these orbits at the Fermi level.

Next, we compare the absolute size of the different k values at the Fermi level extracted from ARPES with those from quantum oscillations (Table I). At low temperatures, ARPES detects a single quasi-two-dimensional hole band [see Fig. 1(k)] along the $\Gamma(Z)$ direction, which has a twofold symmetry, with a maximum area around Z and minimum

around Γ, and a small carrier density of 2.53×10^{20} cm^{-3}. Similarly, ARPES gives clear indication of the presence of an electron-band centered at M, which is a strongly elongated cylinder, but it is lacking the information concerning the behavior of the outer electronlike d_{xy} band crossing the Fermi level, which may be present according to band structure calculations. Since ARPES data suggest that there is only one hole pocket but possibly more than one electron pocket, the largest maximum orbit observed in quantum oscillations, F_4, must corresponds to the hole pocket in order to maintain charge balance in the system; thus two quantum oscillation frequencies with similar effective masses, F_2 and F_4, belong to this quasi-two-dimensional hole band, in close agreement with the size of this quasi-two-dimensional band detected from ARPES [Fig. 1(k)]. Furthermore, the F_3 frequency in quantum oscillations has a substantially larger effective mass than all the other frequencies, which is of similar value to the band renormalization found in the ARPES experiments for the d_{xy} band [γ in Fig. 1(g)], suggesting that *the outer electron pocket that is detected in quantum oscillations but not in ARPES has d_{xy} character*. The inner elongated electron band from ARPES (with areas smaller than 100 T) can be assigned to the F_1 frequencies, as this band is almost two-dimensional (as in seen at the A point in Fig. 5). Thus, by combining the knowledge about the sizes and quasiparticle masses from the ARPES and quantum oscillations data, we suggest that bulk FeSe at low temperatures has one hole and two-electron bands, as represented schematically in Fig. 4. There are some small discrepancies in the absolute values of the cross section areas extracted from ARPES and quantum oscillations, but these could be caused by field-induced Fermi surface effects in quantum oscillations or possible surface effects in ARPES. This interpretation is also consistent with the three-band description of a recent magnetotransport study on FeSe [33], in which a very small high mobility carrier was also detected, in agreement with the size of small electron band from our ARPES data. It is important to note that our measured electronic structure of bulk FeSe is similar to that of multilayers of FeSe on SrTiO$_3$, in which the splitting of bands at the M point was wrongly assigned to a possible formation of a spin-density wave [26]. However, the FeSe monolayer is rather different and its electronic and high T_c superconducting state was suggested to be influenced by SrTiO$_3$ substrate [34].

One important finding from our experimental studies of the electronic structure of FeSe is that the band structure calculations significantly overestimate the size of the Fermi surface of FeSe, even in the tetragonal phase as shown in Fig. 8 in the Appendix. Shrinking of Fermi surfaces in other iron-based superconductors has been assigned to the interband coupling to a bosonic mode in LaFePO [35], and/or the strength of the antiferromagnetic correlations close to a quantum critical point in BaFe$_2$(As$_{1-x}$P$_x$)$_2$ [36]. It is clear that in FeSe, the significant shrinking of the Fermi surface, combined with the strong renormalization effects both in ARPES and quantum oscillations as evidenced by the relatively large effective masses of 4–8 m_e and the orbital-dependent correlations (largest for the d_{xy} band) suggest that the electronic correlations significantly affect the electronic structure of FeSe.
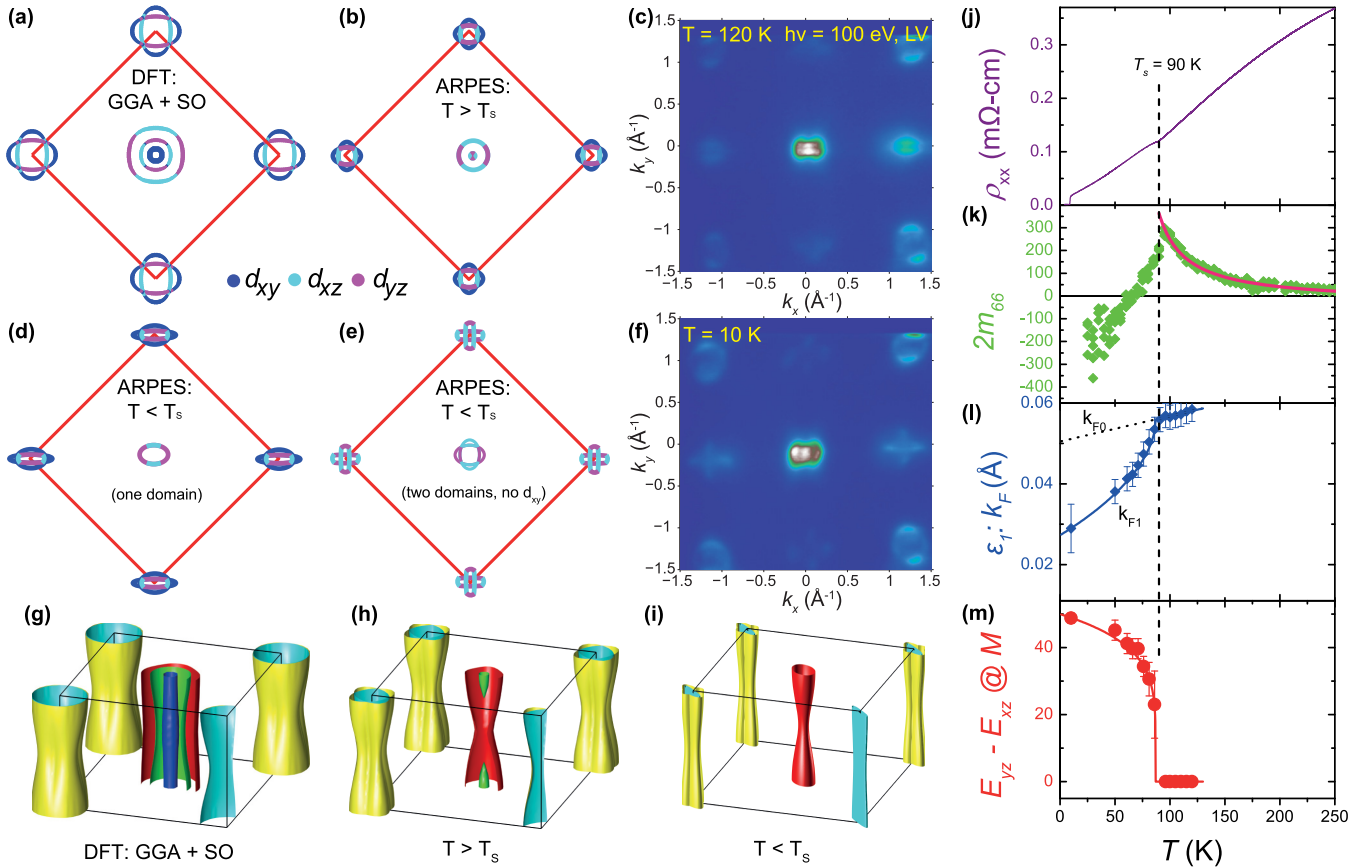
FIG. 4. (Color online) Symmetry-breaking of the electronic structure of FeSe. (a) Band-structure calculation of the Fermi surface in the high-temperature $P4/nmm$ tetragonal space group. (b) Schematic and (c) the experimental high-temperature in-plane Fermi surface consists of significantly shrunk pockets. (d) Elongated hole and electron pockets below the structural transition. (e) Schematic and (f) experimental low-temperature Fermi surface including the effect of twin domains (the d_{xy} electron pocket is not plotted here). (g)–(i) Three-dimensional representations of Fermi surface of FeSe, as described in a, b, and d, respectively. (j) Resistivity as a function of temperature for the sample used in Fig. 3. (k) The induced change in resistivity to in-plane strain measured by the m_{66} parameter from elastoresistance tensor in FeSe, which provides a direct measure of the electronic nematic order parameter, indicating that the structural transition is electronically-driven, as discussed in the main text. (l) Temperature dependence of the intense k_{F1} for the ϵ pocket around the M point, showing the Fermi surface deformation which onsets at T_s. (m) Energy splitting of the bands with d_{xz} and d_{yz} band character at the M point, extracted from Fig. 2(e).

VI. THE NEMATIC SUSCEPTIBILITY OF FeSe

A clear manifestation of a nematic Fermi surface is its strong in-plane anisotropy in transport properties and sensitivity to external parameters, in particular in-plane strain. The resistivity anisotropy is determined by both the electronic structure and the scattering, and the expected Fermi surface deformation give rise naturally to anisotropic electronic properties, whereas the spin-nematic ordering leads to an anisotropy of the electron scattering [4].

Figure 4(k) shows the induced change in resistivity in response to an in-plane strain, given by the $2m_{66}$ component of the elastoresistance tensor in FeSe, which provides a direct measure of the electronic nematic order parameter, as detailed in Fig. 9 and in Ref. [5]. We observe a large increase in $2m_{66}$ approaching T_s, similar to large divergent behavior observed in Ba(Fe/Co)$_2$As$_2$ [4,5], but of even larger magnitude. The data on FeSe can be well described by a fit to the function $2m_{66} = A/(T - T^*) + A_0$, which gives $T^* = 66(1)$ K and

$A_0 = -31(3)$ [solid line in Fig. 4(k)]. Recently, nematic susceptibility measurements of the elastic shear modulus, which probe the lattice response to strain, suggest that the structural transition in FeSe is accompanied by a large shear-modulus softening, identical to that of underdoped Ba(Fe,Co)$_2$As$_2$, implying a very similar strength of the electron-lattice coupling, which is much smaller than the electronic response [14].

The sign of m_{66} is also opposite to what is found in the electron-doped pnictides, but similar to FeTe [18], where it was found that the resistance along the a (AFM) direction is larger than that along b axis (FM direction) [18]. However, a small sign-change of the in-plane anisotropy was also found for highly hole-doped (Ba/K)Fe$_2$As$_2$ [37]. This may suggest that the positive sign of m_{66} may be either a general feature of chalcogenides, as opposed to most of the pnictides, or it is also possible that the development of the anisotropic properties in all these systems may be driven by a different mechanism.

Below the structural transition, T_s, the behavior of m_{66} is rather striking, having an almost linear temperature

dependence with no sign of saturation, as the degree of ellipticity grows larger [see Fig. 4(l)]; it changes sign around 65 K, which, coincidentally, is the same scale as the value of T^* determined earlier. While the interpretation of nematic susceptibility below T_s may be difficult due to domain formation and the fact that the nematic order parameter now takes a finite value, we suggest that one possible explanation for this crossover may be linked to the development of anisotropic scattering from spin-fluctuations, which become strong *below* T_s [14,15]. A sign change of the in-plane anisotropy has been found between the electron and hole-doped $BaFe_2As_2$ [37], being assigned to differences in the spin fluctuations scattering rates corresponding to different Fermi velocities at the hot spots for electron- and hole-doped systems [37,38]. Magnetotransport studies in FeSe also suggest that anisotropic scattering may develop below T_s [33].

As the size of our measured nematic susceptibility is much larger than the response of the lattice [14], we suggest that the structural transition in FeSe is electronically driven and is an instability of the electronic structure, which breaks tetragonal symmetry, with the lattice orthorhombicity simply responding to these electronic changes. Furthermore, the absence of spin fluctuations above T_s indicates that the structural transition in FeSe is not magnetically driven [14,15]. Thus our resistivity anisotropy measurements favor an orbital/charge ordering scenario, which show a strong splitting of the bands with d_{xz} and d_{yz} orbital character [Fig. 2 and summarized in Fig. 4(m)], and it is likely responsible for the in-plane Fermi surface deformation, which gives rise to significant anisotropy in the in-plane electronic structure.

While the orbital ordering scenario is a likely contender to explain the existing data on FeSe, the Fermi surface deformation and its approximate volume conservation (small changes occur due to the temperature dependence of the lattice parameters) bears the similarities of a d-wave Pomeranchuk instability. An isotropic Fermi liquid in the presence of sufficiently strong interactions was predicted by Pomeranchuk to be unstable [30] and as a signature of this instability the Fermi surface would spontaneously deform, changing its shape or topology to lower its energy and break the rotational symmetry, similar to what is observed in FeSe at the Fermi level. The two scenarios are likely to generate different kinds of pairing interactions either at finite momentum [39] or at zero momentum [40] and future theoretical work will need to address these issues.

In summary, we report a comprehensive study of the development of the nematic phase in FeSe. The Fermi surface of FeSe undergoes a spontaneous distortion from fourfold-symmetric to twofold symmetric elliptical pockets. The symmetry breaking arises from the electronic degrees of freedom and, in the absence of magnetism, it is likely to be caused by orbital ordering in the presence of strong interactions. The elongated Fermi surface causes strongly anisotropic electronic properties and enhanced nematic susceptibility. This nematic electronic phase is that from which superconductivity emerges, which is suggested to have a twofold gap symmetry [41]. While interactions favoring orbital ordering dominate near T_s, magnetic fluctuations grow towards T_c, and may still assist the superconducting pairing. Moreover, the existence of a relatively flat hole band just below the Fermi level at the

M point raises the question if whether the presence of van Hove singularities could also play a role in pairing. Given the observed small and strongly anisotropic Fermi surfaces with low carrier densities, it is perhaps not surprising that the physical properties, including the superconducting and structural transitions are susceptible to external parameters (e.g., pressure, strain, doping) so that controlling these one could turn FeSe into a high-temperature superconductor.

APPENDIX

The Sommerfeld coefficient γ is the coefficient of the linear term of the specific heat at low temperature, which arises from the contribution of the degrees of freedom of the quasiparticles at the Fermi level:

$$c_v = \gamma T = \frac{\pi^2}{3} k_B^2 T g(E_F), \qquad (A1)$$

where $g(E_F)$ is the density of states $g(E)$ evaluated at the Fermi level, summed over all contributing bands. For a two-dimensional system, it can be shown that $g(E)$ is proportional to the effective mass of the 2D band, i.e., $m^* \propto \frac{\partial A}{\partial E} \propto g(E_F)$. For FeSe, we find

$$\gamma = \frac{\pi a^2 k_B^2 N_A}{6\hbar^2} \sum_{bands} m^* = 0.70 \sum_{bands} m^*, \qquad (A2)$$

where γ is in mJ/mol K^2 and m^* is measured in electron masses and the prefactor of 0.70 is related to a number of physical constants, including the lattice parameter a. Therefore an estimate of the specific heat can be made from the experimental quantum oscillations effective masses m^* extracted from the temperature dependence of the amplitude of oscillation in Fig. 3(d) and listed in Table I.

TABLE I. Comparison of the Fermi surface parameters as extracted from ARPES and quantum oscillations experiments. The effective mass m^* is obtained from a fit to the standard Lifshitz-Kosevich formula [42] from the temperature dependence of the amplitude of quantum oscillations [Fig. 3(d)]. The energy shifts ΔE and the band renormalization values, *renorm*, are obtained by comparing the relaxed DFT band structure with the high-temperature ARPES data at 120 K, as shown in the main text and the resulting Fermi surface in Fig. 4(h). Due to the different k_z dependence of the experimental and calculated data between Γ and Z small shifts in these numbers are expected. The notably large shift and renormalization factor for the d_{xy} band indicates that it is the most strongly correlated band. The Fermi velocities, v_F, extracted at 120 K are also listed. The values of the elongated Fermi surface pockets, $k_F (y)$ and $k_F (x)$, extracted from the ARPES data at 10 K allow us to compare their extremal areas, A_k [or the corresponding frequencies, F_{ARPES}, using the Onsager relation, $F = A_k \hbar/(2\pi e)$] with those obtained from quantum oscillations at low temperatures and high magnetic fields. The quantum oscillations frequencies, F(T), and effective masses, m^* (m_e), for our sample S4 and S5 (shown in Fig. 3) are compared with those from Refs. [12,13].

Bands	α (Γ)-h $d_{xz/yz}$	α (Z)-h $d_{xz/yz}$	β (Z)-h $d_{xz/yz}$	γ (Z)-h d_{xy}	δ (M)-e d_{xy}	ϵ (M)-e $d_{xz/yz}$
ARPES	$T = 120$ K					
k_F (Å^{-1})	–	0.126	0.052	–	–	0.057
renorm	–	3.2	2.1	8	–	4.1
ΔE (meV)	–	-224	-273	-320	–	$+156$
v_F (meV Å)	–	320(30)	560(80)	–	–	440(30)
ARPES	$T = 10$ K					
$k_F (y)$ (Å^{-1})	0.033(6)	0.10(6)	–	–	–	0.02(1)
$k_F (x)$ (Å^{-1})	0.077(6)	0.15(6)	–	–	–	0.14(1)
A_k (10^{-3} Å^{-2})	8(2)	49(6)	–	–	–	9(5)
F_{ARPES} (T)	85 (50)	510 (80)	–	–	–	95 (60)
QOs	$T < 2$ K	$B > 19$ T				
Orbits	F_2	F_4	–	–	F_3	F_1
F (T) (S4)	207	660	–	–	530	107
m^* (S4)	4.0(5)	4.0(5)	–	–	–	–
F (T) (S5)	200	664	–	–	568	114
m^* (S5)	4.1(5)	4.7(5)	–	–	6(1)	3.0(5)
A_k (10^{-3} Å^{-2})	19	63	–	–	54	11
QOs - Lit.	$T < 2$ K	$B > 19$ T				
F (T) [12]	200	680	–	–	570	60
m^* (m_e) [12]	4.3(1)	4.2(2)	–	–	7.2(2)	1.9(2)
F (T) [13]	200(10)	660	–	–	580	96(6)
m^* (m_e) [13]	2.0(4)	3.2(6)	–	–	–	0.75(2)

In the case of a quasi-two-dimensional cylinder, there are two extremal areas corresponding to a maximum and a minimum quantum oscillation frequencies, and to estimate the contribution to γ one usually averages their effective masses. Based on our ARPES and quantum oscillations, F_2 and F_4 quantum oscillation frequencies correspond to the α hole pocket (the only one that crosses the Fermi level at low temperatures), which gives a value $\gamma_{hole} = 0.7 \times (4.7 + 4.1)/2 = 3.1(4)$ mJ/mol K^2. Next, the F_3 frequency (a maximum) is assigned to the δ electron pocket, which is the electron d_{xy} band at M (not observed in ARPES); assuming that this band is quasi-two-dimensional, the contribution is $\gamma_{electron1} = 4.2(7)$ mJ/mol K^2. Finally, the small and highly elongated ϵ pocket observed in ARPES is assumed to be quasi-two-dimensional corresponding to the F_1 frequency and gives a contribution of $\gamma_{electron2} = 2.1(4)$ mJ/mol K^2. Therefore the total estimated Sommerfeld coefficient from quantum oscillations is $\gamma_{QO} =$ 9.4(15) mJ/mol K^2, larger than the reported experimental value from specific heat of $\gamma_{Cp} = 5.7$ mJ/mol K^2 [14,43]. This discrepancy could be caused by the magnetic field itself as the specific heat γ_{Cp} has been estimated only, so far, from low-field experiments, much lower than the field window used to extract the values of the effective masses from quantum oscillations. The magnetic field can also be responsible for causing increases in the effective masses which needs to be further investigated. Furthermore, the assumption that FeSe has a perfect two-dimensional Fermi surface may also be not ideal and only by knowing the density of states an accurate comparison between the experimental and theoretical value could be made. However, the combined evidence from ARPES, quantum oscillations and also low-temperature magneto-transport measurements on FeSe [33,44] gives unambiguous evidence that FeSe is composed of one hole and two electron bands.
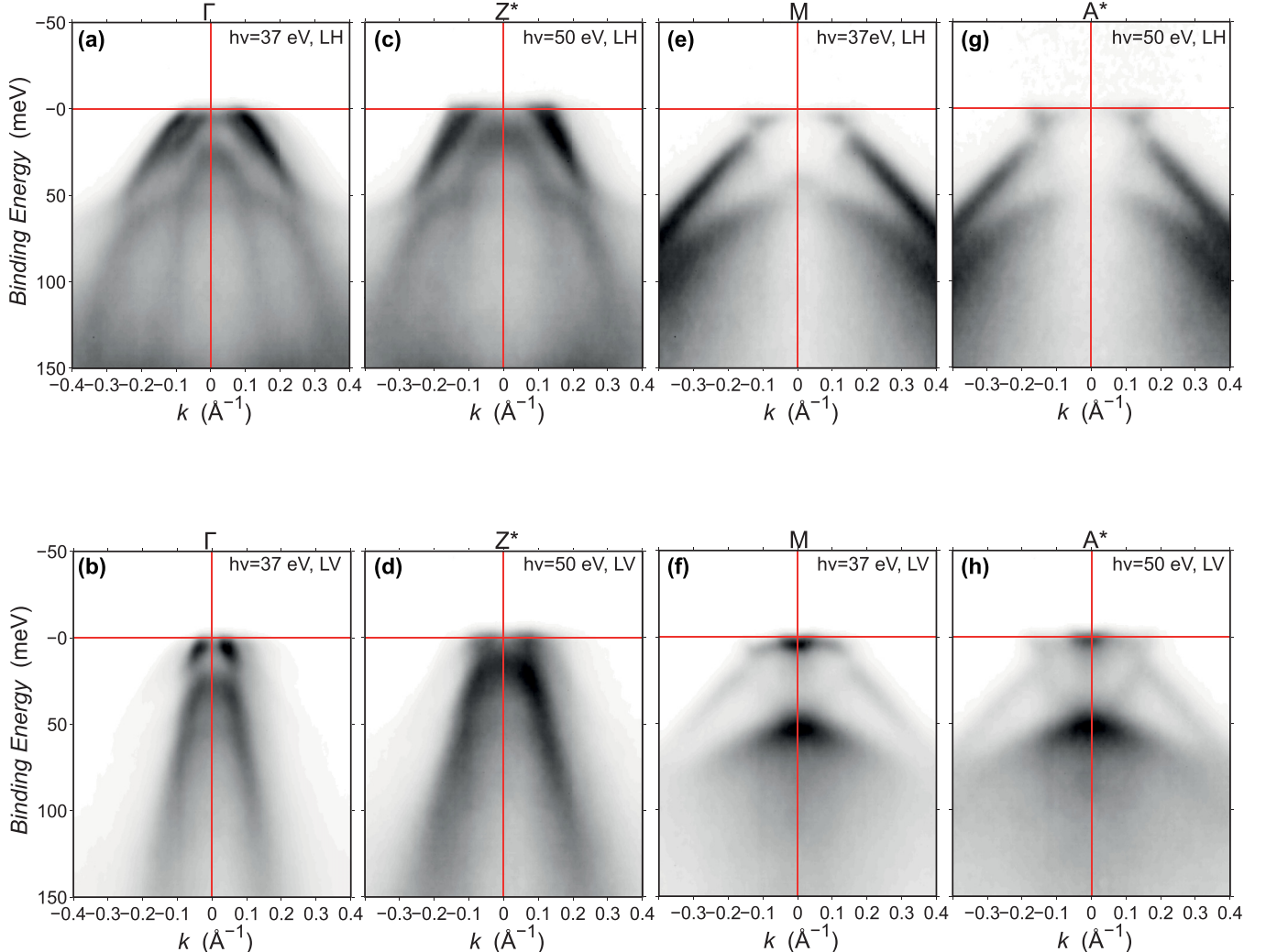
FIG. 5. (Color online) The effect of matrix element effects in ARPES experiments on FeSe at low temperatures. Low-temperature cuts at high-symmetry points in the Brillouin zone performed on an additional sample S3. The measurements were performed for two different incident beam polarizations: linear horizontal, LH,(p) (top row) or linear vertical, LV, (s) (bottom row). All samples measured were carefully aligned such that the Γ-M direction corresponded to the scattering plane (equivalently, the local coordinate frame of the Fe atoms is aligned to the scattering plane). In this geometry, matrix-element effects allow us to select predominantly bands with d_{xz} (LH) or d_{yz} (LV) orbital character. Further details can be found in Ref. [18]. As detailed in Fig. SM2, the spin-orbit coupling mixes the orbital characters of different bands near anticrossings and also at the high-symmetry Γ point and this effects allows the d_{xy} band to be observed near $\Gamma(Z)$ in LH, otherwise the ARPES signal for d_{xy} band due to the matrix elements effects [18] would be very small at Γ, or not even observed, as in the case of the M point (Fig. 2). At the Γ point, there is a mixing of orbital character due to spin-orbit coupling (as described below), as shown in the LV polarization cuts at Γ and Z in (b) and (d). The $Z*$ and $A*$ cuts are performed at 50 eV, which are close to the next symmetry points at the top of the Brilloiun zone besides those at 23 eV shown in Fig. 1(k). The photon energy or the k_z dependence reveals the degree of corrugation of the two-dimensional bands; the hole pocket α around $\Gamma(Z)$ in (a) and (b) is more strongly-corrugated than the electron pocket around M(A) in (f) and (h).
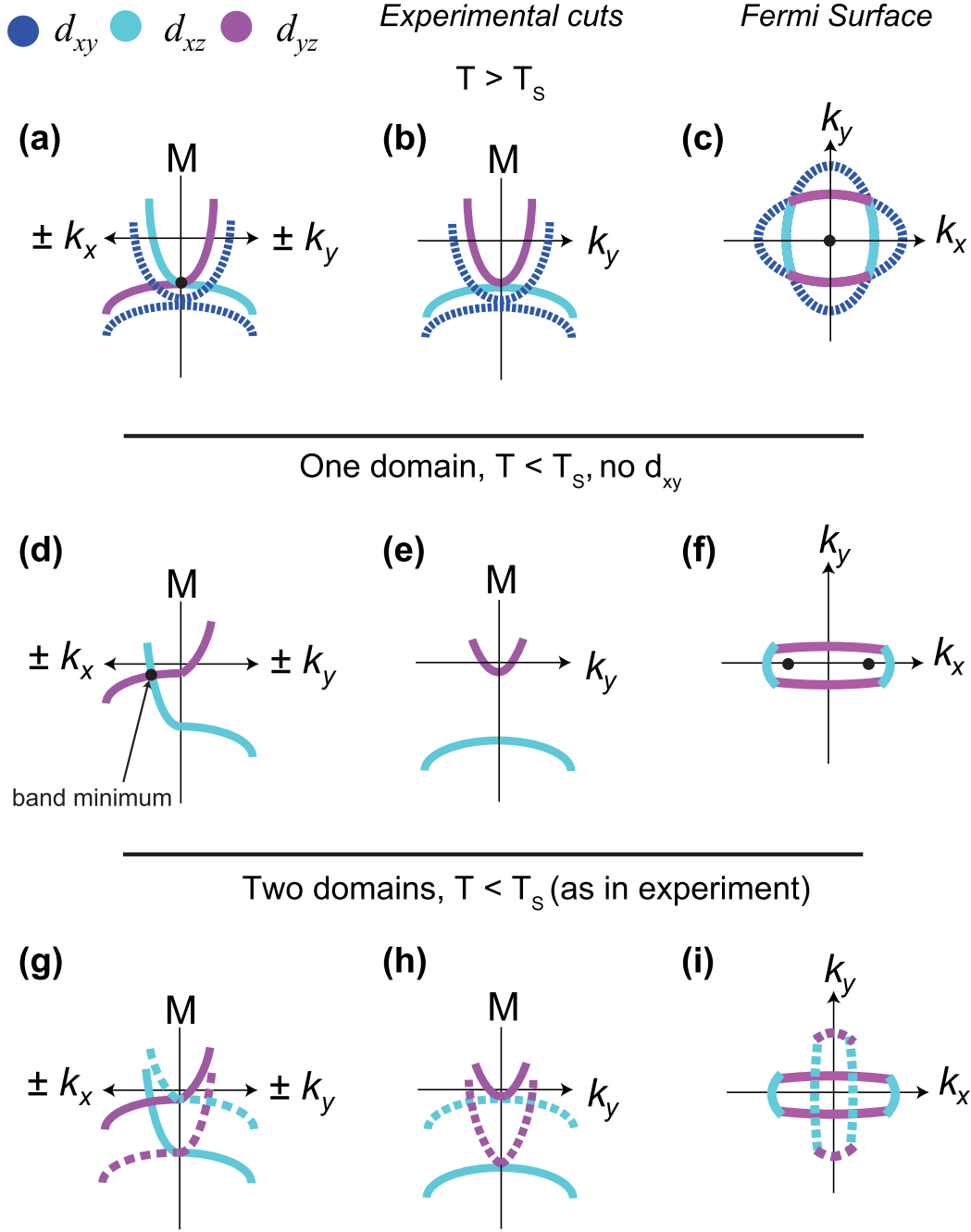
FIG. 6. (Color online) Schematic representation of the development of the dramatic Fermi surface deformation at the *M* point. (a)–(c) Schematic high-temperature cuts and Fermi surface around the *M* point; there is a fourfold degeneracy (even with spin-orbit coupling [19]) of the d_{xz} and d_{yz} bands dispersing along the k_x and k_y directions (similar to a double saddle-point). This degeneracy is lost when the fourfold symmetry of the lattice is broken, and the d_{xz} and d_{yz} bands separate. The d_{xy} band is not observed at the *M* point at any temperature and is therefore shown as a dashed line only in (a)–(c). (d)–(f) Schematic of the low-temperature Fermi surface and high-symmetry cuts for one domain only when the observed pocket becomes highly elongated. The band with d_{yz} orbital character moves up, whereas the d_{xz} band is pushed down away from the Fermi level as suggested by experiments on detwinned crystals from Ref. [11]. The positions of the band crossings (band minima of the band crossing at the Fermi level) are marked by black dots. Consequently, at the Fermi level, the d_{yz} portion of the Fermi surface contracts, whereas the d_{xz} portion expands. (g)–(h) Schematic of the experimental data at *M*, formed by a superposition of dispersions originating from twin domains that are at 90° with respect to each other (solid and dashed lines). The beam spot is sufficiently large that we expect to always observe the superposition of bands in the two structural domains. The contribution of the second domain to the experimental k_y cut is equivalent to the dispersion along k_x but with orbital characters reversed ($x \leftrightarrow y$). Therefore the observed experimental cuts have four observed dispersions that result in a cross-shapes Fermi surfaces in Figs. 2 and 4 of the main text. Although the d_{xy} band is not observed at the *M* point in ARPES, we can assign the F_3 frequency in quantum oscillations with the heaviest mass to the d_{xy} pocket, which needs to break the rotational symmetry, similar to the other pockets.
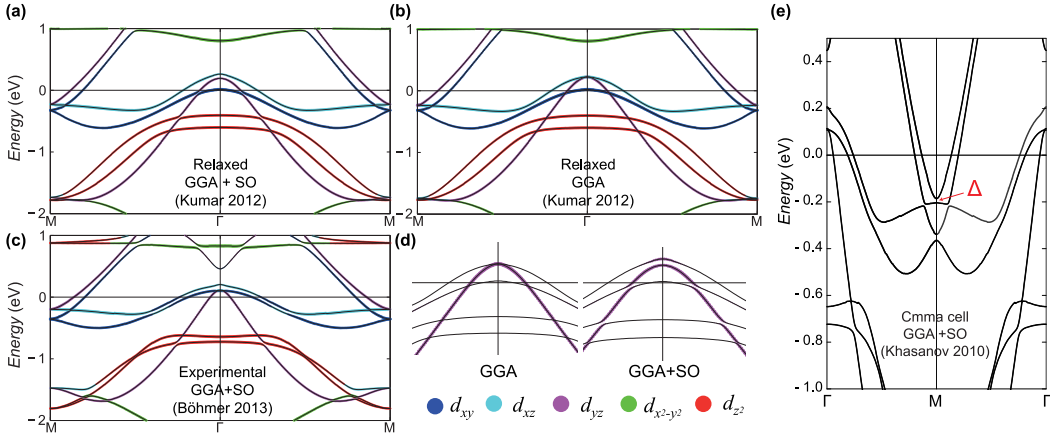
FIG. 7. (Color online) Band-structure calculations of FeSe using relaxed and experimental structures. (a) Band structure calculations performed using WIEN2K [45] based on the relaxed crystal structure of Ref. [16] and including spin-orbit coupling. A comparison to a calculation without spin-orbit coupling is presented in (b) where there are no spin-orbit induced band anti-crossings, and additionally the d_{xz} and d_{yz} orbitals are degenerate at Γ. (c) Calculation based on the experimental structure reported in Ref. [9], including spin-orbit coupling. The main difference between the two crystallographic structures in (a) and (c) is the Se position, z_{Se}, above the Fe plane, significantly shorter for the relaxed structure, $z_{\text{Se}} = 0.241\,28$ [16], as compared with the experimental one, $z_{\text{Se}} = 0.266\,68$ [9]). (d) Detailed cuts of the relaxed structure near the Γ point showing only the d_{yz} weight. As well as lifting the degeneracy at the Γ point, spin-orbit coupling mixes the orbital characters of bands near anticrossings and also at the high-symmetry Γ point. (e) Calculation of band dispersion in the low-temperature *Cmma* space group (when the fourfold rotational symmetry is broken) taking the structure of Ref. [46]. A splitting of bands at the M point is now allowed and is calculated to be 17 meV, in the absence of any band renormalization effects.
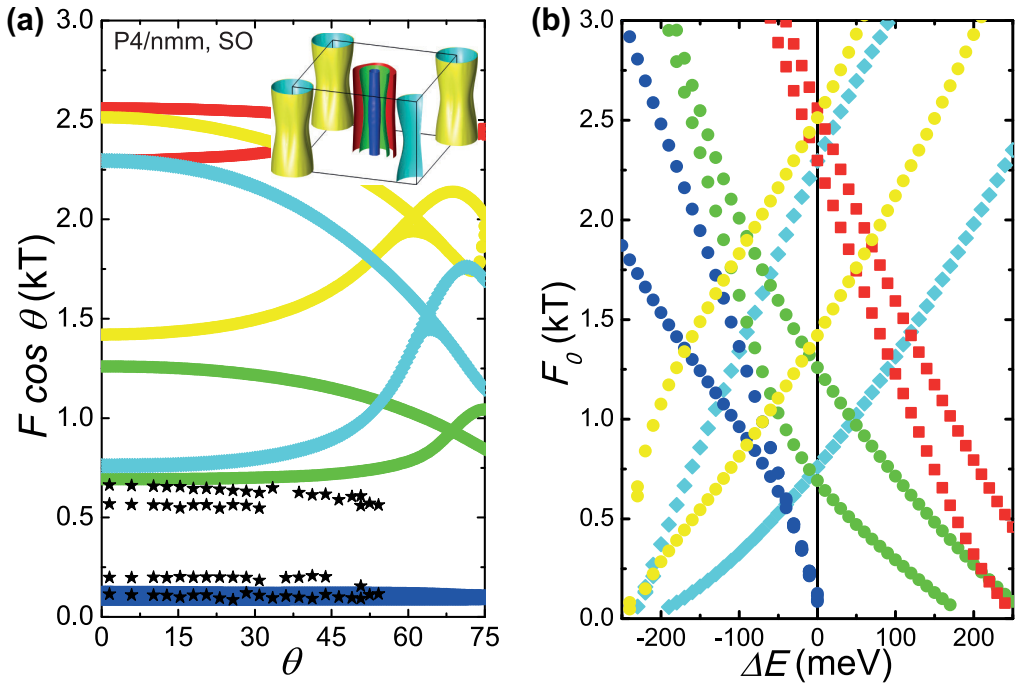

FIG. 8. (Color online) Comparison between the predicted and measured values of quantum oscillations frequencies. (a) Predictions of quantum oscillation frequencies as a function of angle in FeSe, using the $P4/nmm$ relaxed structure of Ref. [16]. θ is defined as the angle of rotation from the c axis to the a axis. Black stars are experimental data points. Inset: corresponding Fermi surface. The predicted quantum oscillation frequencies (calculated using the SKEAF algorithm [47]) consists of frequencies up to $\sim$2.6 kT arising from quasi-2D bands. The calculation are performed for the high-temperature tetragonal phase; in the orthorhombic paramagnetic case, by including the small structural distortion, 2×10^{-3}, we find very little difference to the shape of the Fermi surface or predicted quantum oscillations frequencies. (b) Calculated quantum oscillation frequencies at $\theta = 0$ as a function of rigid band shift. Large shifts of $\sim$200 meV would be required to bring the calculated frequencies down to the order of the experimental frequencies. Like in other iron-based superconductors, the ground state in DFT of FeSe is not a paramagnetic state but a collinear antiferromagnetic stripe-order, with other possible magnetic orders close in energy [16]. Studies of quantum oscillations of the magnetically ordered phase typically reveal small pockets, originated from a reconstructed Fermi surfaces [48,49]. A magnetically reconstructed Fermi surface would produced frequencies of comparable sizes to those observed in FeSe, however, FeSe does not undergo any magnetic transition and our ARPES measurements do not show any evidence of band folding to support this scenario.
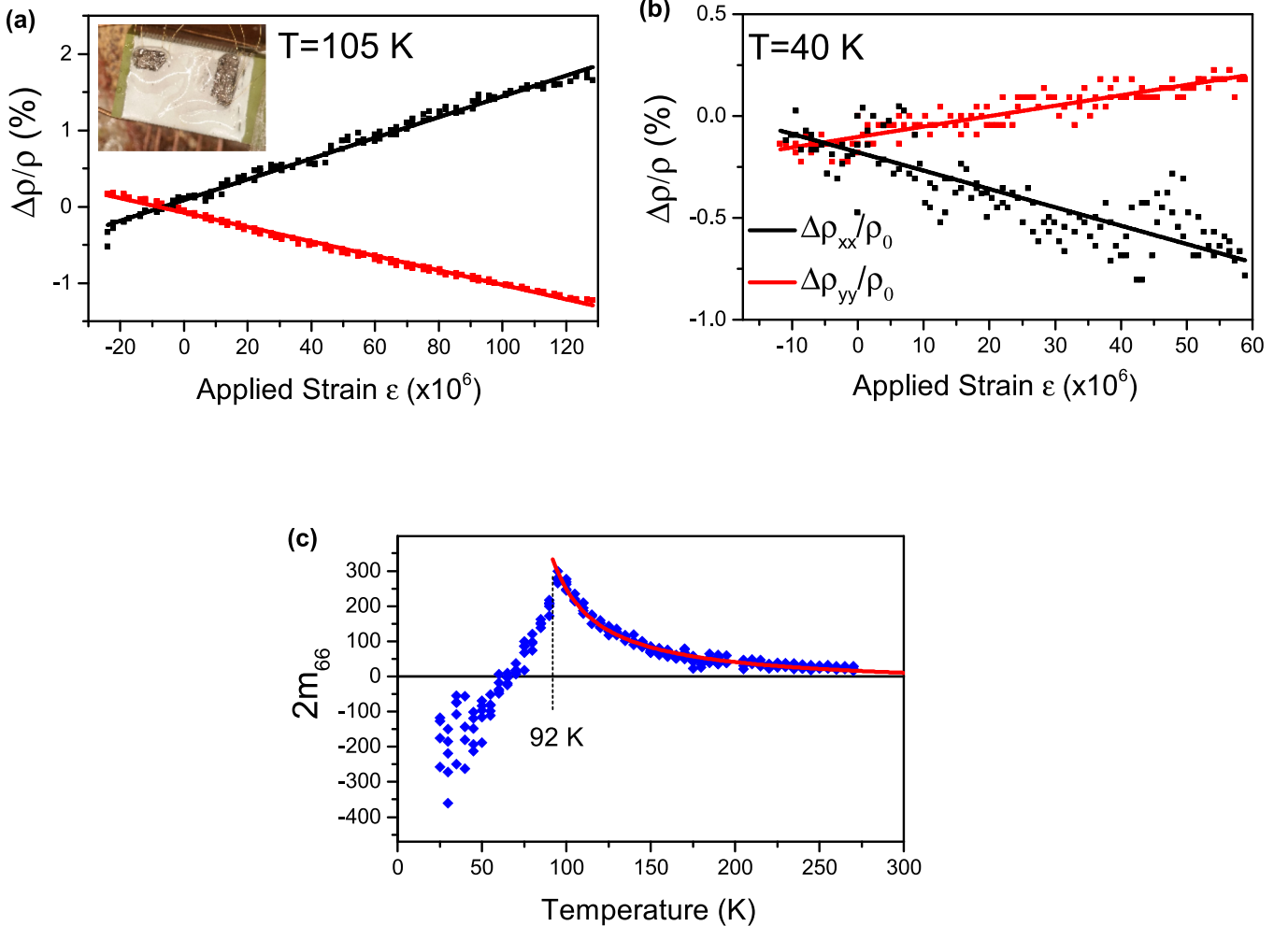
FIG. 9. (Color online) Elastoresistance measurements of FeSe. Elastoresistivity measurements as a function of temperature at (a) 105 and (b) 40 K, with strain induced by a varying voltage to a piezoelectric stack, as discussed in detail in Ref. [5]. Samples were bonded to the top surface of the piezostack with the crystallographic [110] $_{\text{tetragonal}}$ axis (checked with x-ray diffraction) parallel or perpendicular to the piezostack long axis, as shown in the inset. Resistive strain gauges were bonded to the bottom surface of the piezostack to monitor the applied strain by sweeping the voltage applied to the piezostack. Due to the biaxial strain of the piezostack, the fractional change in resistivity, $\Delta\rho/\rho_0$ (normalised to the zero-strain value ρ_0), were made either perpendicular (ρ_{xx}) or parallel (ρ_{yy}) to the piezostack long axis; ϵ_{xx} and ϵ_{xx} is the uniaxial strain component along the perpendicular and the parallel directions, respectively. There is a sign change as a function of temperature for $\Delta\rho/\rho_0$ in (a) and (b). (c) The variation of the elastoresistance tensor component, m_{66}, as a function of temperature. The $2m_{66}$ parameter is the ratio between the subtracted parallel (yy) and perpendicular (xx) components of the fractional change in resistivity and the applied strained, being defined as $2m_{66} = (\Delta\rho_{xx}/\rho_0 - \Delta\rho_{yy}/\rho_0)/(\epsilon_{xx} - \epsilon_{yy})$, as detailed in Ref. [5]. The m_{66} increases dramatically towards the structural transition, which in this experimental set up is at $\sim$92 K. The solid line corresponds to a fit to the function $m_{66} = A/(T - T^*) + A_0$, which gives $T^* \sim 66(1)$ K and $A_0 = -31(3)$. There is an unusual sign change of m_{66} as a function of temperature below 65 K, as discussed in the main text.

[1] E. Fradkin, S. A. Kivelson, M. J. Lawler, J. P. Eisenstein, and A. P. Mackenzie, Ann. Rev. Condens. Matter Phys. **1**, 153 (2010).

[2] R. M. Fernandes, A. V. Chubukov, and J. Schmalian, Nat. Phys. **310**, 97 (2014).

[3] W. Lv, J. Wu, and P. Phillips, Phys. Rev. B **80**, 224506 (2009).

[4] J.-H. Chu, H.-H. Kuo, J. G. Analytis, and I. R. Fisher, Science **337**, 710 (2012).

[5] H.-H. Kuo, M. C. Shapiro, S. C. Riggs, and I. R. Fisher, Phys. Rev. B **88**, 085113 (2013).

[6] S. Medvedev, T. M. McQueen, I. A. Troyan, T. Palasyuk, M. I. Eremets, R. J. Cava, S. Naghavi, F. Casper, V. Ksenofontov, G. Wortmann, and C. Felser, Nat. Mater. **8**, 630 (2009).

[7] M. Burrard-Lucas, D. G. Free, S. J. Sedlmaier, J. D. Wright, S. J. Cassidy, Y. Hara, A. J. Corkett, T. Lancaster, P. J. Baker, S. J. Blundell, and S. J. Clarke, Nat. Mater. **12**, 15 (2013).

[8] J.-F. Ge, Z.-L. Liu, C. Liu, C.-L. Gao, D. Qian, Q.-K. Xue, Y. Liu, and J.-F. Jia, Nat. Mater. **14**, 285 (2014).

[9] A. E. Böhmer, F. Hardy, F. Eilers, D. Ernst, P. Adelmann, P. Schweiss, T. Wolf, and C. Meingast, Phys. Rev. B **87**, 180505 (2013).

[10] K. Nakayama, Y. Miyata, G. N. Phan, T. Sato, Y. Tanabe, T. Urata, K. Tanigaki, and T. Takahashi, Phys. Rev. Lett. **113**, 237001 (2014).

[11] T. Shimojima, Y. Suzuki, T. Sonobe, A. Nakamura, M. Sakano, J. Omachi, K. Yoshioka, M. Kuwata-Gonokami, K. Ono, H. Kumigashira, A. E. Böhmer, F. Hardy, T. Wolf, C. Meingast, H. v. Löhneysen, H. Ikeda, and K. Ishizaka, Phys. Rev. B **90**, 121111 (2014).

[12] T. Terashima, N. Kikugawa, A. Kiswandhi, E.-S. Choi, J. S. Brooks, S. Kasahara, T. Watashige, H. Ikeda, T. Shibauchi, Y. Matsuda, T. Wolf, A. E. Böhmer, F. Hardy, C. Meingast, H. v. Löhneysen, M.-T. Suzuki, R. Arita, and S. Uji, Phys. Rev. B **90**, 144517 (2014).

[13] A. Audouard, F. Duc, L. Drigo, P. Toulemonde, S. Karlsson, P. Strobel, and A. Sulpice, Europhys. Lett. **109**, 27003 (2015).

[14] A. E. Böhmer, T. Arai, F. Hardy, T. Hattori, T. Iye, T. Wolf, H. Löhneysen, K. Ishida, and C. Meingast, Phys. Rev. Lett. **114**, 027001 (2015).

[15] S.-H. Baek, D. V. Efremov, J. M. Ok, J. S. Kim, J. van den Brink, and B. Büchner, Nat. Mater. **14**, 210 (2015).

[16] J. Kumar, S. Auluck, P. K. Ahluwalia, and V. P. S. Awana, Supercond. Sci. Technol. **25**, 095002 (2012).

[17] J. Maletz, V. B. Zabolotnyy, D. V. Evtushinsky, S. Thirupathaiah, A. U. B. Wolter, L. Harnagea, A. N. Yaresko, A. N. Vasiliev, D. A. Chareev, A. E. Böhmer, F. Hardy, T. Wolf, C. Meingast, E. D. L. Rienks, B. Büchner, and S. V. Borisenko, Phys. Rev. B **89**, 220506 (2014).

[18] Y. Zhang, C. He, Z. R. Ye, J. Jiang, F. Chen, M. Xu, Q. Q. Ge, B. P. Xie, J. Wei, M. Aeschlimann, X. Y. Cui, M. Shi, J. P. Hu, and D. L. Feng, Phys. Rev. B **85**, 085121 (2012).

[19] V. Cvetkovic and O. Vafek, Phys. Rev. B **88**, 134510 (2013).

[20] S. Borisenko, D. Evtushinsky, I. Morozov, S. Wurmehl, B. Buchner, A. Yaresko, T. Kim, and M. Hoesch, arXiv:1409.8669.

[21] A. Tamai, A. Y. Ganin, E. Rozbicki, J. Bacsa, W. Meevasana, P. D. C. King, M. Caffio, R. Schaub, S. Margadonna, K. Prassides, M. J. Rosseinsky, and F. Baumberger, Phys. Rev. Lett. **104**, 097002 (2010).

[22] Z. P. Yin, K. Haule, and G. Kotliar, Phys. Rev. B **86**, 195141 (2012).

[23] Z. R. Ye, Y. Zhang, F. Chen, M. Xu, J. Jiang, X. H. Niu, C. H. P. Wen, L. Y. Xing, X. C. Wang, C. Q. Jin, B. P. Xie, and D. L. Feng, Phys. Rev. X **4**, 031041 (2014).

[24] N. Lanatà, H. U. R. Strand, G. Giovannetti, B. Hellsing, L. de' Medici, and M. Capone, Phys. Rev. B **87**, 045122 (2013).

[25] S. Mandal, R. E. Cohen, and K. Haule, Phys. Rev. B **89**, 220502 (2014).

[26] S. Tan, Y. Zhang, M. Xia, Z. Ye, F. Chen, X. Xie, R. Peng, D. Xu, Q. Fan, H. Xu, J. Jiang, T. Zhang, X. Lai, T. Xiang, J. Hu, B. Xie, and D. Feng, Nat. Mater. **12**, 634 (2013).

[27] M. Yi, D. Lu, J.-H. Chu, J. G. Analytis, A. P. Sorini, A. F. Kemper, B. Moritz, S.-K. Mo, R. G. Moore, M. Hashimoto, W.-S. Lee, Z. Hussain, T. P. Devereaux, I. R. Fisher, and Z.-X. Shen, Proc. Natl. Acad. Sci. **108**, 6878 (2011).

[28] M. Yi, D. H. Lu, R. G. Moore, K. Kihou, C.-H. Lee, A. Iyo, H. Eisaki, T. Yoshida, A. Fujimori, and Z.-X. Shen, New J. Phys. **14**, 073019 (2012).

[29] C. He, Y. Zhang, B. P. Xie, X. F. Wang, L. X. Yang, B. Zhou, F. Chen, M. Arita, K. Shimada, H. Namatame, M. Taniguchi, X. H. Chen, J. P. Hu, and D. L. Feng, Phys. Rev. Lett. **105**, 117002 (2010).

[30] I. I. Pomeranchuk, JETP Lett. **35**, 524 (1958).

[31] A. I. Coldea, J. D. Fletcher, A. Carrington, J. G. Analytis, A. F. Bangura, J.-H. Chu, A. S. Erickson, I. R. Fisher, N. E. Hussey, and R. D. McDonald, Phys. Rev. Lett. **101**, 216402 (2008).

[32] C. Putzke, A. I. Coldea, I. Guillamón, D. Vignolles, A. McCollam, D. LeBoeuf, M. D. Watson, I. I. Mazin, S. Kasahara, T. Terashima, T. Shibauchi, Y. Matsuda, and A. Carrington, Phys. Rev. Lett. **108**, 047002 (2012).

[33] M. D. Watson, T. Yamashita, S. Kasahara, W. Knafo, M. Nardone, F. Beard, F. Hardy, A. McCollam, A. Narayanan, S. F. Blake, T. Wolf, A. A. Haghighirad, C. Meingast, A. J. Schofield, H. v. Löhneysen, Y. Matsuda, A. I. Coldea, and T. Shibauchi, arXiv:1502.02922.

[34] J. J. Lee, F. T. Schmitt, R. G. Moore, S. Johnston, Y.-T. Cui, W. Li, M. Yi, Z. K. Liu, M. Hashimoto, Y. Zhang, D. H. Lu, T. P. Devereaux, D.-H. Lee, and Z.-X. Shen, Nature **515**, 245 (2014).

[35] L. Ortenzi, E. Cappelluti, L. Benfatto, and L. Pietronero, Phys. Rev. Lett. **103**, 046404 (2009).

[36] H. Shishido, A. F. Bangura, A. I. Coldea, S. Tonegawa, K. Hashimoto, S. Kasahara, P. M. C. Rourke, H. Ikeda, T. Terashima, R. Settai, Y. Ōnuki, D. Vignolles, C. Proust, B. Vignolle, A. McCollam, Y. Matsuda, T. Shibauchi, and A. Carrington, Phys. Rev. Lett. **104**, 057008 (2010).

[37] E. C. Blomberg, M. A. Tanatar, R. M. Fernandes, I. I. Mazin, B. Shen, H.-H. Wen, M. D. Johannes, J. Schmalian, and R. Prozorov, Nat. Commun. **4**, 1914 (2013).

[38] M. Breitkreiz, P. M. R. Brydon, and C. Timm, Phys. Rev. B **90**, 121104 (2014).

[39] H. Kontani and S. Onari, Phys. Rev. Lett. **104**, 157001 (2010).

[40] C. J. Halboth and W. Metzner, Phys. Rev. Lett. **85**, 5162 (2000).

[41] C.-L. Song, Y.-L. Wang, P. Cheng, Y.-P. Jiang, W. Li, T. Zhang, Z. Li, K. He, L. Wang, J.-F. Jia, H.-H. Hung, C. Wu, X. Ma, X. Chen, and Q.-K. Xue, Science **332**, 1410 (2011).

[42] D. Shoenberg, *Magnetic Oscillations in Metals* (Cambridge University Press, Cambridge, 1984).

[43] J.-Y. Lin, Y. S. Hsieh, D. A. Chareev, A. N. Vasiliev, Y. Parsons, and H. D. Yang, Phys. Rev. B **84**, 220507 (2011).

[44] K. K. Huynh, Y. Tanabe, T. Urata, H. Oguro, S. Heguri, K. Watanabe, and K. Tanigaki, Phys. Rev. B **90**, 144516 (2014).

[45] P. Blaha, K. Schwarz, G. Madsen, D. Kvasnicka, and J. Luitz, WIEN2K (Techn. Univ. Wien, Austria, 2001).

[46] R. Khasanov, M. Bendele, K. Conder, H. Keller, E. Pomjakushina, and V. Pomjakushin, New J. Phys. **12**, 073024 (2010).

[47] P. Rourke and S. Julian, Comput. Phys. Commun. **183**, 324 (2012).

[48] S. E. Sebastian, J. Gillett, N. Harrison, P. H. C. Lau, D. J. Singh, C. H. Mielke, and G. G. Lonzarich, J. Phys. Condens. Matter **20**, 422203 (2008).

[49] T. Terashima, N. Kurita, M. Tomita, K. Kihou, C.-H. Lee, Y. Tomioka, T. Ito, A. Iyo, H. Eisaki, T. Liang, M. Nakajima, S. Ishida, S.-i. Uchida, H. Harima, and S. Uji, Phys. Rev. Lett. **107**, 176402 (2011).